Fracture Mechanics of Concrete Structures
Proceedings FRAMCOS-3
AEDIFICATIO Publishers, D-79104 Freiburg, Germany

A STUDY OF COMPRESSIVE FAILURE IN OVER-REINFORCED CONCRETE BEAMS

H.D. Kang, E. Spacone, and K.J. Willam,
CEAE Department, University of Colorado at Boulder, USA

Abstract

The failure behavior of under- and in particular of over-reinforced concrete beams depends not only on strength, but to a large extent, on the ductility and softening behavior of concrete in compression.

Recently, a 3-D finite element formulation was presented at the University of Colorado for the failure assessment of R/C members. Parallel to that effort, a sophisticated analysis capability for R/C-frames is under development based on a flexibility-based fiber representation of the cross-section which accounts for shear deformations, bond slip, and transverse confinement. The purpose of this study is to compare the predictions of the 3-D concrete model, with the results of the layered beam-column element when an over-reinforced concrete beam is considered. To this end the benchmark problem specified by RILEM Technical Committee 148 SSC *'Strain Softening of Concrete'* is used to study the issue, whether the fracture energy argument of tensile cracking does also hold for localized failure in compression.

Key words: Compressive failure, 1-D and 3-D FE analysis of over-R/C beam.

1 Introduction

The vulnerability of highway bridges to earthquake ground motions was very apparent in a number of major earthquakes, such as the 1971 San Fernando, the 1989 Loma Prieta, and the 1994 Northridge earthquakes (Seismic Advisory Board) in California, and the recent 1995 Hyogoken-Nanbu earthquake (EERI, 1995) in Japan. Bridge structures which were severely damaged in the Hyogoken-Nanbu earthquake, were designed with older code provisions, lacking specific detailing requirements to ensure sufficient ductility of the piers. While most of the catastrophic failures of reinforced concrete bridge piers in that earthquake can be attributed to inadequate confinement or transverse reinforcement, the damage induced in numerous oversized piers is still difficult to perceive without detailed engineering analysis. This includes severe bending and crushing failures, as well as brittle diagonal shear failures which took place in many oversized piers.

A research project is carried out at the University of Colorado at Boulder to explain some of the failure phenomena of bridge piers in the Hygoken-Nanbu earthquake. This paper describes the on-going effort in terms of a flexibility-based fiber model for beam-column analysis (Spacone et al., 1996), and in terms of a three-dimensional finite element analysis with a triaxial constitutive model for concrete (Kang et al., 1997), to capture diffuse and localized failure modes under different triaxial load scenarios. To illustrate the performance of the two models with a specific softening problem of great interest, the nonlinear behavior of an over-reinforced concrete beam is studied which was tested at the Technical University Aalborg, Denmark (Ulfkjær et al., 1997) in conjunction with the benchmark problem specified by RILEM Technical Committee 148 SSC. The ACI/ASCE Committee 447 on *'Finite Element Analysis of Reinforced Concrete Structures'* does participate in this round-robin test in order to evaluate the predictive capabilities of state-of-the-art finite elements to capture compressive failure of concrete due to softening not only in tension but also in compression. The paper summarizes first results of the over-reinforced concrete beam which will eventually be compared with experimental data on the benchmark problem that have not been made public for obvious reasons.

2 Fiber model analysis of over-reinforced R/C beam

The first part of this paper studies the performance of the flexibility-based fiber elements proposed by Spacone et al. (1996), to capture the response of an over-reinforced concrete beam (Ulfkjær et al. 1997). Two geometrically similar reinforced concrete beams were tested in the benchmark study. Only the larger beam is considered in this paper. The specimen dimensions and reinforcement are shown in Figures 1 and 2. The beam is simply supported with a clear span of 7200 mm, depth 400 mm and thickness 200 mm. The beam is made of normal strength concrete with nine 20 mm-diameter ribbed bars at the bottom and two bars at the top. The beam has been tested in four-point loading, with loads applied at 600 mm from midspan. To force compression failure of the beam, the top reinforcement was interrupted at approximately 300 mm from midspan (Figure 1). The compressive strength of the normal strength concrete was 22.75 MPa and the yield stress for the reinforcing bars was 650 MPa.

The goal of the joint experimental/analytical research outlined in Ulfkjær et al. (1997) is to investigate whether current modeling techniques, in combination with standard test data on strain softening of concrete under mode I and uniaxial compression, are sufficient to correctly predict the behavior of over-reinforced concrete beams.

The beam of Figure 1 was initially studied by using the fiber beam element depicted in Figure 2. The element is based on the classical assumption that plane sections remain plane and normal to the longitudinal axis of the element. The element is formulated by following the force approach, and assumes constant axial load and linear bending moment diagrams inside the element. The element is very accurate because the assumed force distributions are 'exact', in the sense that the internal forces satisfy pointwise equilibrium with the nodal forces. The element is numerically robust and has been successfully used to simulate the response of softening R/C columns under large axial forces.

The element idealization of the beam structure in Figure 1 is shown in Figure 2. Due to the symmetry of beam and loads, only half of the beam was discretized into four nodes and three elements. The first beam element extends from the support to the point where

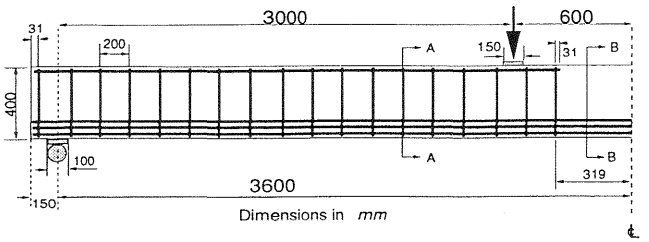

Figure 1. Over-reinforced concrete beam.

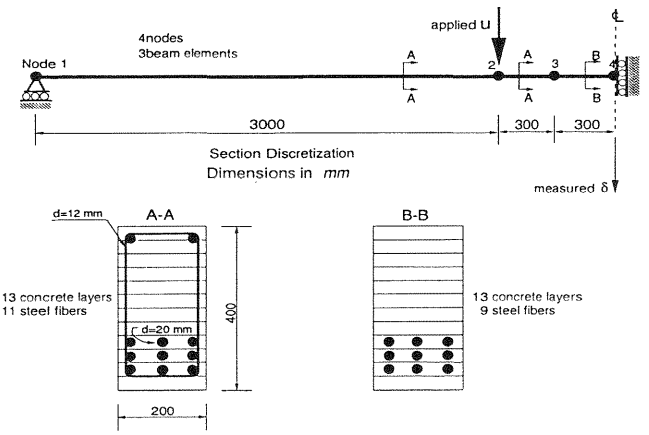

Figure 2. FE mesh of over-reinforced concrete beam & section discretization into layers.

the load is applied in displacement control. The second element extends until the point where the top reinforcement is interrupted, and the third element extends to midspan. The section discretization into layers is shown at the bottom of Figure 2. Thirteen concrete layers were used. More refined section discretizations do not show substantial changes in the results. Elements 1 and 2 have the same cross section with both top and bottom reinforcement (Section A-A), while element 3 has no top reinforcement (Section B-B). The uniaxial constitutive law for concrete is based on the Kent-Park model (Kent and Park, 1971). The law is shown in the inset of Figure 3. It is a parabola from the origin to the point of maximum strength (ϵ_{c0}, f'_c), followed by a softening straight line that terminates where the line reaches a residual compressive strength of 20% f'_c at a strain called ϵ_{cu}. For larger compressive strains the residual strength remains constant. This model is important for understanding of the results of the numerical study. For the current study, the peak strength $f'_c = 22.75\ MPa$

was at a strain $\epsilon_{c0} = 0.0014$, while different values of the slope of the softening curve were used. The tensile strength of concrete was neglected in this study which concentrates on the compression behavior of the beam. As for the steel, the Menegotto-Pinto model was used (Menegotto et al., 1973). Following the data in Ulfkjær et al. (1997), the initial stiffness was $E_s = 222,000\ MPa$ and the yield stress $f_y = 650\ MPa$. A very small strain hardening modulus was used. An initial study of the problem showed that neither the number of elements nor the number of integration points per element selected in the constant moment region have any influence on the beam response. The bending moment is constant in this region, and any number of force-based elements are capable of capturing the constant moment solution. The only parameter that influences on the beam response is the softening branch of the concrete stress-strain relationship.

The results of the numerical study are shown in Figure 3. The figure plots the applied load P versus the vertical deflection δ measured at midspan. The results are shown for three values of concrete softening. Higher values of the ultimate concrete strain, ϵ_{cu} (the strain at which the stress reaches a residual strength of 20% f'_c) not only induce more ductile response, but also increase the beam strength. A comparison between the uniaxial compression test on normal strength concrete (from Ulfkjær et al. 1997) and the model by Kent-Park sheds more insight on the analyses. First of all, an accurate representation of the strength and ductility (f'_c, ϵ_{c0}) leads to overestimating the initial modulus of elasticity of the material, because of the parabolic formulation shown in the ascending branch of the stress-strain relations. It is therefore expected that the elastic stiffness of the numerical analysis will be higher than that observed in the experimental test. As for the descending branch, the residual strength of the model is 20% f'_c, which appears to be higher than the experimental value. Finally, three slopes were selected for the descending branch. For a value of $\epsilon_{cu} = 0.00575$ the descending slope is very steep, as shown in Figure 3. Smaller values of ϵ_{cu} cause snap-back in the response, thus this case was not considered in the beam study. Figure 4 shows the stress response of four fibers versus the displacement at midspan δ for the case with $\epsilon_{cu} = 0.00575$. The

extreme concrete fiber in compression (labeled 'concrete 1') reaches its strength at a displacement of approximately 30 mm and then gradually looses the strength. The three steel layers are initially in tension, but for large displacement the upper layer (labeled 'steel 1') goes into compression, indicating that the neutral axis moves below 'steel 1'. When the concrete in compression is severely crushed, the section is reduced to the bottom steel only, and for equilibrium to be maintained some of the steel must be in compression.

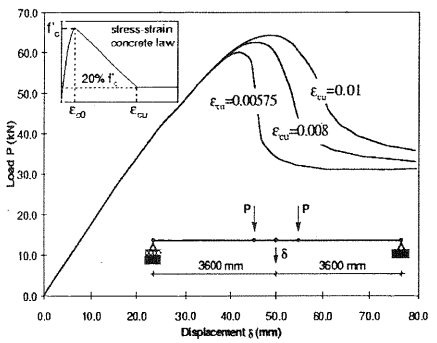

Figure 3. Applied load *vs.* midspan deflection.

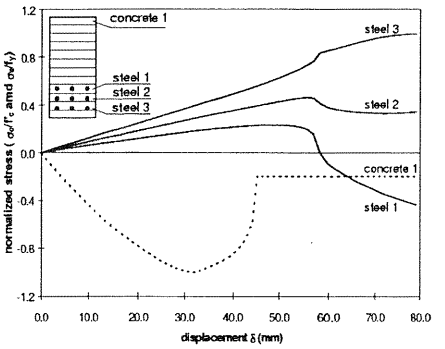

Figure 4. Midspan section: normalized fiber stress *vs.* midspan deflection.

Subsequently, a numerical study was performed to assess whether the beam model suffers from localization due to a numerical imperfection. The beam of Figure 2 was tested using a concrete with the same properties of Figure 1, but with $\epsilon_{cu} = 0.05$. The beam was studied first without a numerical imperfection and then with a reduced concrete compressive strength $f'_c = 22.74\ MPa$ at the last integration point of element 3. The analyses were repeated for 2, 3 and 4 integration points. The results of Figure 5 clearly indicate that this small imperfection suffices to cause strain localization at the last integration point, and the overall effect on the post-peak response increases with the number of integration points. This behavior is illustrated in more detail in Figure 6, that shows the moment-curvature response of element 3 with two integration points. While section 2 (the one with $f'_c = 22.74\ MPa$) reaches the peak and then softens, section 1 (the one with $f'_c = 22.75\ MPa$) does not quite reach the peak and unloads elastically. The analyses of Figures 5 and 6 were performed

with $f_c' = 22.74\ MPa$ throughtout the last integraton point. The test was then repeated by setting $f_c' = 22.74\ MPa$ only in the extreme concrete fiber in compression in the last integration point. Localization and loss of mesh objectivity were observed in this case, too. It should be pointed out the beam element used for the analyses uses Gauss-Lobatto quadrature points, thus the first and last integration points always coincide with the two end sections of the element. The results of this analysis clearly show that beam elements with softening behavior suffer from strain localization similar to the ones observed in solid finite elements.

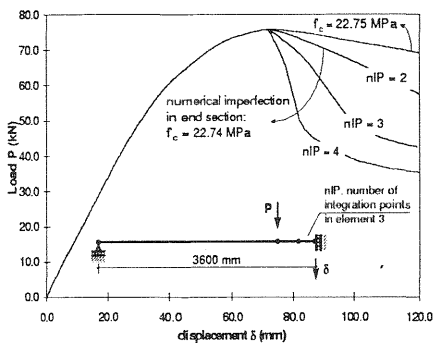

Figure 5. Beam analysis with a numerical imperfection at the last integration point of element 3.

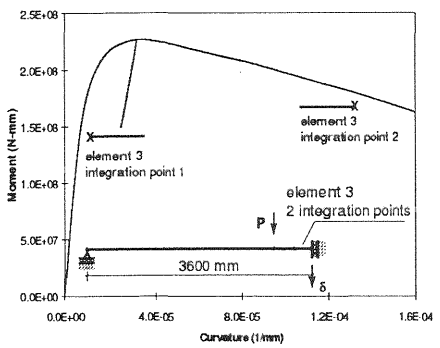

Figure 6. Section response for analysis with two integration points.

3. Three dimensional study

3.1 Triaxial concrete model

The triaxial concrete model proposed by Kang (1997) is based on an elasto-plastic constitutive formulation in which the initial yield surface and the failure envelope bound the hardening regime of concrete in tension and compression, respectively. After the stress path reaches the failure envelope, the concrete model exhibits strain softening under progressive straining in triaxial tension, and perfect plasticity under high confined compression. Hence, the concrete model captures both hardening and softening in compression and tension. A non-associated flow rule plays a significant role in characterizing

plastic dilatation in order to assure realistic predictions of inelastic volume changes at different confinement levels. The main features of the novel concrete model and its distinction from other existing models are briefly summarized below.

3.1.1 Elasto-Plastic Formulation

Based on standard flow theory of elasto-plasticity the strain rate decomposes additively into an elastic component and a plastic component, $\dot{\epsilon} = \dot{\epsilon}_e + \dot{\epsilon}_p$ in the case of infinitesimal deformations. The elastic strain rate is related to the stress rate by Hooke's law:

$$\dot{\sigma} = \mathcal{E} : \dot{\epsilon}_e = \mathcal{E} : (\dot{\epsilon} - \dot{\epsilon}_p) \tag{1}$$

where $\mathcal{E} = \Lambda \boldsymbol{\delta} \otimes \boldsymbol{\delta} + 2G\mathcal{I}$ denotes the isotropic elasticity tensor. Assuming that there is no elastic damage the elastic properties remain constant during the entire plastic deformation process. The elastic range is delimited by the plastic yield condition, $F(\boldsymbol{\sigma}, q_h, q_s) = 0$, the size and shape of which depend on two internal variables q_h, q_s, one for describing the increase of strength due to hardening and one for describing the degradation of strength due to tensile softening. In the case of plastic loading, the direction of the plastic strain rate is governed by the non-associated flow rule:

$$\dot{\epsilon}_p = \dot{\lambda} \frac{\partial Q}{\partial \boldsymbol{\sigma}} = \dot{\lambda}\, \boldsymbol{m} \tag{2}$$

where Q denotes the plastic potential and $\dot{\lambda}$ the plastic multiplier. The latter is determined with the help of the plastic consistency condition, $F_{n+1}(\Delta\lambda) = 0$, which assures that the constitutive behavior under persistent plastic deformations is consistent within the finite time interval $\Delta t = t_{n+1} - t_n$.

3.1.2 Yield Function

The curvilinear loading surface $F(\boldsymbol{\sigma}, q_h, q_s) = 0$ maintains C^1-continuity except for the apex in equitriaxial tension. The deviatoric sections of the triaxial failure envelope in Figure 7 have a triangular shape in tension and low confined compres-

Figure 7. Deviatoric Sections

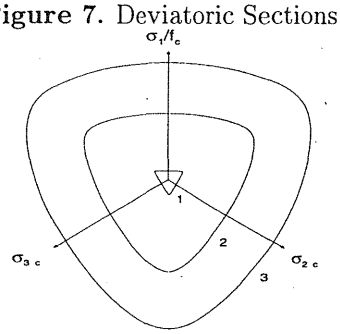

sion which gradually transforms into a circular shape under increasing hydrostatic pressure.

3.1.2.1 *Strain Hardening*

In the hardening regime, the plastic yield condition

$$F(\xi,\rho,\theta,k(q_h,\xi)) = \rho r(\theta,e) - \rho_1\{\left(\frac{\xi-\xi_o}{\xi_1-\xi_o}\right)^{\alpha} + \left(\frac{\xi-\xi_1}{\xi_o-\xi_1}\right)^{\beta(k)} - 1\} \quad = 0 \qquad (3)$$

is a function on the Haigh-Westergaard stress coordinates, and thus the three stress invariants, $\xi = \frac{I_1}{\sqrt{3}}$, $\rho = \sqrt{2J_2}$, $\theta = \frac{1}{3}\cos^{-1}\left(\frac{3\sqrt{3}}{2}\frac{J_3}{\sqrt{J_2}}\right)$. Hardening is controlled by the normalized hardening variable $k = k(q_h,\xi)$ which varies between $0 \leq k \leq 1$, where q_h corresponds to the equivalent plastic strain, and where ξ introduces the effect of hydrostatic stress on the nonlinear hardening response. The exponent α accounts for the pressure-sensitivity of the triaxial concrete strength, where for instance $\alpha = 0.5$ spans a failure surface in the form of a triple symmetric paraboloid.

Strain hardening is governed by the exponent $\beta(k)$ in the loading function in Eqn. 3, where

$$\beta(k) = 0.25\frac{(1-k^2)}{(1-k_o{}^2)} \qquad (4)$$

is a function of the hardening parameter, $k = k(q_h,\xi)$, where

$$\begin{aligned} k(q_h,\xi) &= \frac{2}{h_D(\xi)}(1-k_0)(\sqrt{2h_D(\xi)q_h} - q_h) + k_0 \\ h_D(\xi) &= A_h\cdot(\frac{\xi}{f_c'})^2 + B_h(\frac{\xi}{f_c'}) + C_h \end{aligned} \qquad (5)$$

According to Eqn. 4, the exponent $\beta(k)$ in the hardening term of the yield function varies from 0.25 to zero as $k_o \leq k \leq 1$. When $\beta = 0$, the compression cap fully opens up and the compressive meridian (corresponding to $\theta = 60^o$) of the loading surface reaches the failure envelope as depicted in Figure 8(a). Thereby the compressive meridian of the failure surface passes through the point of uniaxial compression.

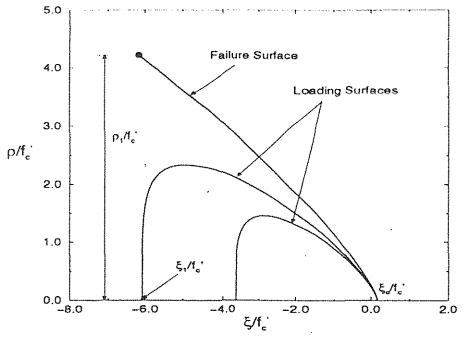

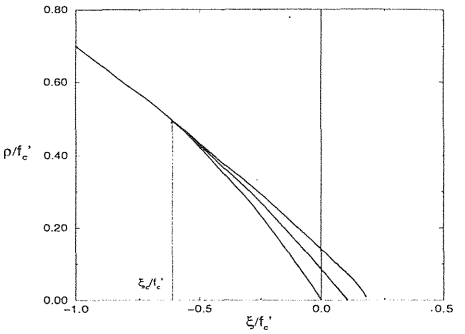

Figure 8 (a) Strain Hardening Meridians. (b) Strain Softening Meridians.

3.1.2.2 *Strain Softening*

When the stress path reaches the failure surface, then the hardening exponent $\beta \rightarrow 0$, and the hardening term becomes inactive. Progressive straining in triaxial tension mobilizes softening of the yield condition in Eqn. 6 which is augmented by the normalized decohesion variable $1 \geq c(q_s, \xi) \geq 0$:

$$F(\xi, \rho, \theta, c(q_s, \xi)) = \rho r(\theta, e) - \rho_1 \{ \left(\frac{\xi - \xi_o}{\xi_1 - \xi_o} \right)^{\alpha} - (1 - c) \left(\frac{\xi_o}{\xi_o - \xi_1} \right)^{\alpha} \left(\frac{\xi_c - \xi}{\xi_c} \right)^2 \} = 0 \qquad for\ \xi \geq \xi_c \tag{6}$$

Note, $\xi_c = -T\xi_o$ locates the transition point of brittle/ductile fracture below which softening takes place. For $\xi \leq \xi_c$, the yield surface coincides with the failure envelope, and therefore, the behavior of the material is perfectly plastic in that regime. The change of the loading surface due to strain softening is illustrated in Figure 8(b), whereby the strain softening parameter $c = c(q_s, \xi)$ controls tensile degradation as a function of the equivalent tensile fracture strain, q_s and the hydrostatic pressure, ξ:

$$c(q_s, \xi) = \frac{1}{exp\ \left[\delta (\frac{q_s \ell_c}{s_D(\xi)})^2 \right]} \tag{7}$$

where, $\dot{q}_s = \dot{\lambda} \| \boldsymbol{m}_t \|_2$, $s_D(\xi) = A_s(\xi - B_s \cdot f_t^{'})^4 + 1$. The internal softening variable is activated by the equivalent tensile fracture strain, q_s from the time when the stress path reaches the failure envelope. Thereby $\boldsymbol{m}_t$ extracts only tensile components from the gradient of the

plastic potential $\boldsymbol{m}$, ℓ_c denotes the characteristic length for fracture energy-based strain softening, and $s_D(\xi)$ accounts for the influence of the confinement pressure on the slope of the softening branch. The value of the strain softening variable $1 \leq c(q_s, \xi) \leq 0$ varies according to the state of decohesion from one to zero.

3.1.3 Plastic Potential

A non-associated flow rule is adopted for realistic predictions of concrete dilatation at different levels of confinement. The plastic potential has the same structure as Eqns. 4 and 6, but with the exponent α being replaced by $\bar{\alpha}$. Experimental data on concrete materials indicate that $0 < \bar{\alpha} < \alpha$.

3.2 A single element study of concrete failure in axial compression

In order to investigate the failure mechanism of the over-reinforced concrete beam, a single 3-D finite element is used to study compression failure under representative boundary conditions. First of all, the tensile test data (Ulfkjær et al. 1997) are compared to the numerical prediction of the concrete model, the calibration of which was adjusted by setting $f_c' = 22.75\ MPa$. The fracture energy of 165.0 N/m in the numerical simulation of the tension test with a single brick element shows a value which is about 1.7 times higher than the energy of 97.09 N/m in the experiment. Figure 9 illustrates the difference of ductility/toughness in uniaxial tension, since the concrete model in Section 3.1 had previously been calibrated with the aid of low strength triaxial tension and compression data (Hurlbut, 1985). The parameter values in-use are summarized in Table 1. Since the constitutive model is formulated in terms of normalized quantities, i.e. $\frac{\xi}{f_c'}$ & $\frac{\rho}{f_c'}$, the parameters are independent of specific units.

Table 1: Parameter Values of Concrete Model

f_c' (MPa)	ξ_o (MPa)	α	S	A_h	B_h
22.75	4.5	0.77	7.0	-0.000283	-0.00572
C_h	T	A_s	B_s	δ	$\bar{\alpha}$
0.000424	8.2	0.000222	0.65818	$10^{4.3}$	0.23

The local compressive behavior of the over-reinforced concrete

beam under four-point bending is studied for two different conditions: (a) plain concrete under uniaxial compression representing the unreinforced mid-section of the beam, and (b) reinforced concrete under axial compression with steel ratios $\rho_x = 1.65\%$, $\rho_y = 0.3\%$, *and* $\rho_z = 0.57\%$, representative for sections near the loading point with axial rebars and stirrups. Thereby, the 3-D simulations are carried out on a single brick element, when plain concrete under axial compression is compared with the results of reinforced concrete. The uniaxial compression test denoted here as the plane stress case is idealized with the help of a single brick element and lateral stress-free boundary conditions ($\sigma_y = 0$). The axial compression test denoted here as the plane strain case imposes an out-of-plane deformation constraint ($\epsilon_y = 0$).

(a) Figure 10 illustrates the compressive stress-strain response behavior of the plain concrete model under uniaxial compression (plane stress), and the experimental data in low/high friction case by Ulfkjær et al.(1997). As expected from the tension test in Figure 9, the softening branch of the numerical predictions show more ductile behavior than the test data. The tendency of diffuse axial splitting is indicated in Figure 13(a), and the variation of the normalized localization tensor $\boldsymbol{Q}_{ep} = \boldsymbol{N} \cdot \boldsymbol{\mathcal{E}}_{ep} \cdot \boldsymbol{N}$ *versus* $\boldsymbol{N}$ is shown in Figure 14 in terms of the angle θ. The polar plot of the eigenvalues, $\lambda_i = \rho c_i^2$ of the localization tensor $\boldsymbol{Q}_{ep}$, represent shear/longitudinal wave velocities, c_{ij} in Figure 15. Whereby the shear eigenvalue (inner circle) degraded along two shear directions of $\theta \sim \pm 30^o$, and the in-plane longitudinal eigenvalue decreased in the form of an axial splitting mode where $\theta = 0^o$. Thus combined with the result in Figure 14, it is noted that mixed compression-shear failure is likely to develop at the beginning of softening, but that axial splitting eventually dominates failure at the end of the softening branch, where all results in Figures 13, 14, and 15 are evaluated at the terminal point of the post-peak behavior. They clearly illustrate diffuse failure in the direction of axial splitting. Consequently, the cylindrical stress state in uniaxial compression leads to loss of stability (Hill, 1958), i.e. $d^2W = 0$ marked by the symbol, • in the stress-strain diagram without localization.

In contrast, in plane strain, the in-plane response exhibits a local-

ized failure mode depicted in Figures 13(b) and 14, which occurs at $\theta = 31^o,\ 149^o$. Figure 11 demonstrates that the localization (marked by the symbol, $\oplus$) takes place in the ascending branch due to lack of normality in non-associated flow. In contrast the value of the second order work density only vanishes at the peak of the hardening process which is stabilized by the out-of-plane confinement effect. It is interesting that the induced out-of-plane stress σ_y reaches 10 % of the axial stress as shown in Figure 11. When compared to the unconfined case of plane stress, the plane strain constraint however breaks the symmetry of the cylindrical stress state in uniaxial compression, and enhances the axial strength by 10 % above the uniaxial compressive strength $f_c' = 22.75\ MPa$. Note, the confinement effects are relatively small because of the non-associated flow rule used in the elastoplastic concrete model.

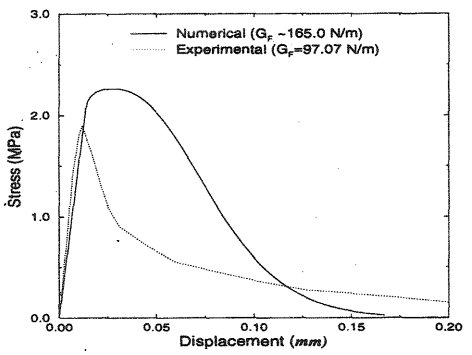

Figure 9. Uniaxial Tension.

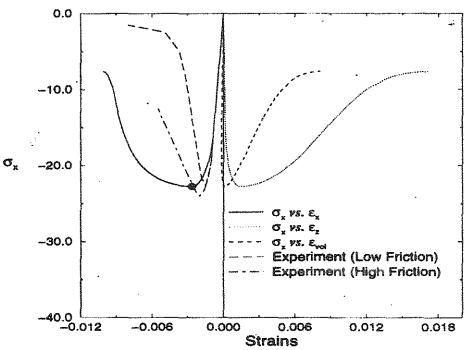

Figure 10. Uniaxial Compression.

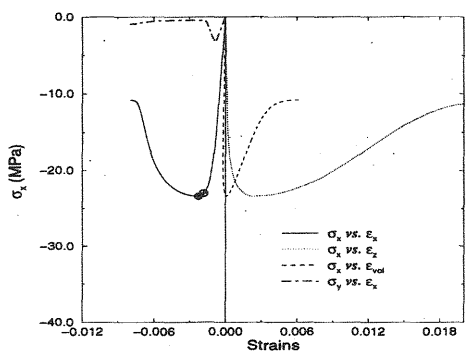

Figure 11. Axial Compression (Plane Strain).

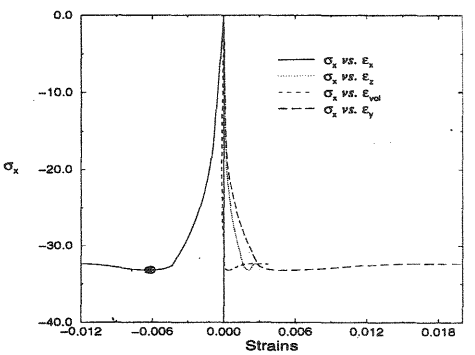

Figure 12. Axial Compression (Reinforced concrete for $\rho_y \neq \rho_z$)

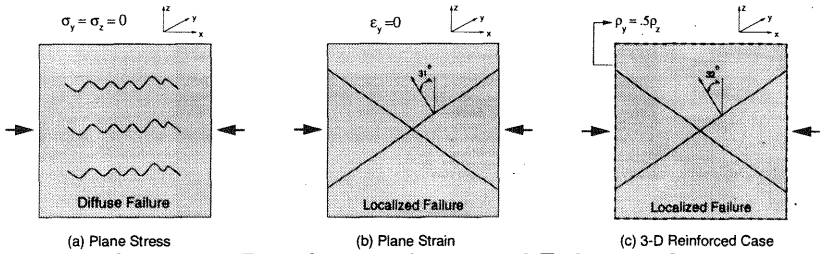

Figure 13. Boundary conditions and Failure modes in (a) Plane stress, (b) Plane strain, and (c) 3-D reinforced concrete.

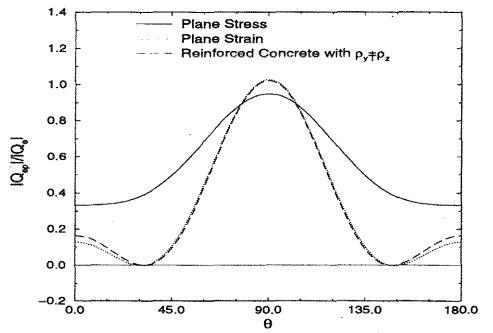

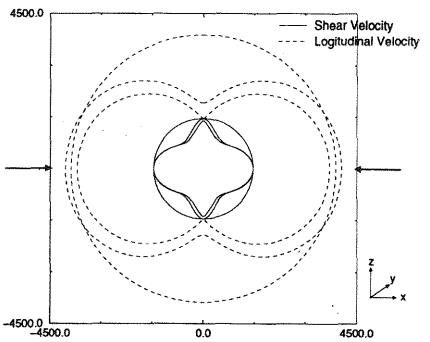

Figure 14. Localization Anaysis. **Figure 15.** Polar plots of phase velocities in uniaxial compression (Plane Stress)

(b) For completeness, the effect of axial and transverse reinforcement is examined in uniaxial compression. To this end, the concrete brick element is reinforced by distinct rebars along the edges according to the reinforcement ratios $\rho_y = 0.3\%$, $\rho_z = 0.57\%$. The reinforced concrete element results in significantly higher strength and ductility values depicted in Figure 12, since failure develops only when the axial and transverse steel bars reach yielding. Similarly to the plane strain case, localization analysis in Figures 13(c), and 14 indicates that the slight difference in transverse reinforcement ($\rho_y < \rho_z$) leads to localized failure. This failure mode differs fundamentally from the diffuse non-localized failure mode in axial compression (Kang, 1997) of reinforced concrete columns with axial rebars and an equal amount of stirrups in both lateral directions ($\rho_y = \rho_z$). In the current study the different amount of transverse steel in y- and z-directions induces different transverse confinement which breaks symmetry of the cylindrical stress state, and eventually

leads to localization. Figure 12 illustrates the two distinct lateral response curves in the y- and z-directions.

4. Conclusions

The analysis of an over-reinforced concrete beam showed the capabilities and limitations of the fiber formulation when the R/C beam is failing in compression. The element is 'stress-based', thus a very few elements are required to obtain a converged equilibrium solution. The results of the over-reinforced beam showed that not only is the response sensitive to the softening slope, but strain localization due to small imperfections can also develop. To study the extremes of one- versus two- and three-dimensional analyses a triaxial concrete model was introduced to explore the compressive failure of plain and reinforced concrete. The model accounts for the effect of lateral confinement on the behavior of concrete in terms of stiffness, strength and ductility. The triaxial concrete model was subjected to a number of compression tests which did illustrate the strong influence of confinement. For the 3-D simulation of compression failure of the entire over-reinforced concrete beam, further studies are needed to capture the compressive failure under a variety of different geometry (size effect) and concrete properties (normal, high strength, and fiber-reinforced concrete).

Acknowledgments

The first and last author gratefully acknowledge the partial support of this study by the AFOSR, Grant No. F49620-98-1-0159 under liaison of Maj. Mike Chipley. Opinions expressed in this paper are of the writers and do not necessarily reflect those of the sponsor.

5. References

Hurlbut, B.J. (1985) Experimental and Computational Investigation of Strain-Softening in Concrete. **M.S. Thesis**, University of Colorado, Boulder.

EERI., The Hyogo-Ken Nanbu Earthquake - January 17, 1995. Re-

port No. 95-04, **Earthquake Engineering Research Institute**, Oakland.

Hill, R. (1958) A General Theory of Uniqueness and Stability in Elastic-Plastic Solids., **Mechanics and Physics of Solids** 6, 236-249.

Kang, H. (1997) Triaxial Constitutive Model for Plain and Reinforced Concrete Behavior, **Ph.D. Dissertation**, CEAE Department, University of Colorado Boulder, Boulder.

Kang, H. and Willam, K (1997) Computational Issues of Concrete Failure. Proc. **Advanced Design of Concrete Structures**, K. Gylltoft, B. Engström, L.-O. Nilsson, N.-E. Wiberg and P. Ahman eds., CIMNE, Barcelona, 15-29.

Kent, D.C. and Park, R. (1971) Flexural Members with Confined Concrete. **J. Struct. Div., ASCE**, 97(ST7), 1964-1990.

Menegotto, M., and Pinto, P. E. (1973) Method of Analysis for Cyclically Loaded Concrete Plane Frames Including Changes in Geometry and Nonelastic Behavior of Elements under Combined Normal Force and Bending. IABSE Symp. on **Resistance and Ultimate Deformability of Structures Acted on by well-defined Repeated Loads**, Final Report, Lisbon, Portugal.

Seismic Advisory Board., The Continuing Challenge - The Northridge Earthquake of January 17, 1994., Report to the Director, **California Department of Transportation**, Sacramento.

Spacone, E., Filippou, F.C., and Taucer, F.F. (1996) Fiber Beam-Column Model for Nonlinear Analysis of R/C Frames. I: Formulation. **Earthquake Engineering and Structural Dynamics**, 25 (7), 711-725.

Ulfkjær, J.P., van Mier, J.G.M., and Stang, H. (1997) Invitation to a competition on: Modeling of Over-Reinforced Concrete Beams. RILEM Technical Committee 148 SSC **Strain Softening of Concrete** and ACI/ASCE Committee 447 on **Finite Element Analysis of Reinforced Concrete Structures**.